ARTICLES
PUBLISHED ONLINE: 24 JUNE 2012 | DOI: 10.1038/NPHYS2351
nature physics

Hedgehog spin texture and Berry's phase tuning in a magnetic topological insulator

Su-Yang Xu[1], Madhab Neupane[1], Chang Liu[1], Duming Zhang[2], Anthony Richardella[2], L. Andrew Wray[1,3], Nasser Alidoust[1], Mats Leandersson[4], Thiagarajan Balasubramanian[4], Jaime Sánchez-Barriga[5], Oliver Rader[5], Gabriel Landolt[6,7], Bartosz Slomski[6,7], Jan Hugo Dil[6,7], Jürg Osterwalder[7], Tay-Rong Chang[8], Horng-Tay Jeng[8,9], Hsin Lin[10], Arun Bansil[10], Nitin Samarth[2] and M. Zahid Hasan[1,11]*

Understanding and control of spin degrees of freedom on the surfaces of topological materials are key to future applications as well as for realizing novel physics such as the axion electrodynamics associated with time-reversal (TR) symmetry breaking on the surface. We experimentally demonstrate magnetically induced spin reorientation phenomena simultaneous with a Dirac-metal to gapped-insulator transition on the surfaces of manganese-doped Bi_2Se_3 thin films. The resulting electronic groundstate exhibits unique hedgehog-like spin textures at low energies, which directly demonstrate the mechanics of TR symmetry breaking on the surface. We further show that an insulating gap induced by quantum tunnelling between surfaces exhibits spin texture modulation at low energies but respects TR invariance. These spin phenomena and the control of their Fermi surface geometrical phase first demonstrated in our experiments pave the way for the future realization of many predicted exotic magnetic phenomena of topological origin.

Since the discovery of three-dimensional topological insulators[1–5] (TI), topological order proximity to ferromagnetism has been considered as one of the core interests of the field[6–16]. Such interest is strongly motivated by the proposed TR breaking topological physics such as the quantized anomalous chiral Hall current, spin current, axion electrodynamics, and the inverse spin-galvanic effect[9–12], all of which critically rely on finding a way to break TR symmetry on the surface and use the unique TR broken spin texture for applications. As quantum coherence is essential in many of these applications, devices need to be engineered into thin films to enhance or de-enhance surface-to-surface coupling or the quantum tunnelling of the electrons. The experimental spin behaviour of surface states under the two extreme limits, namely the doped magnetic groundstate and ultrathin film quantum tunnelling groundstate, is thus of central importance to the entire field. However, surprisingly, it is not known what happens to the spin configuration under these extreme conditions relevant for device fabrication. Fundamentally, TR symmetry is inherently connected to the Kramers' degeneracy theorem, which states that when TR symmetry is preserved, the electronic states at the TR invariant momenta have to remain doubly spin degenerate. Therefore, the establishment of the TR breaking effect fundamentally requires measurements of electronic groundstate with a spin-sensitive probe. Here we use spin-resolved angle-resolved photoemission spectroscopy (ARPES) to measure the momentum space spin configurations in systematically magnetically doped, non-magnetically doped, and ultrathin quantum coherent TI films[17], to understand the nature of electronic groundstates under the two extreme limits vital for magnetic topological devices. These measurements allow us to make definitive conclusions regarding magnetism on topological surfaces, and make it possible to quantitatively isolate the TR breaking effect in generating the surface electronic gap from many other physical or chemical changes also leading to gap-like behaviour[18–22] often observed on the surfaces. Spin reorientation measurements and the systematic methodology demonstrated here can be used to probe quantum magnetism on the surfaces of other materials as well.

Topological surface states with magnetic doping

To study the evolution of topological surface states on magnetic doping, magnetically (Mn%) and (chemically similar) non-magnetically (Zn%) doped Bi_2Se_3 thin films are prepared in high quality using the molecular beam epitaxy (MBE) growth method. A sample layout and a photographic image of a representative MBE-grown film used for experiments are shown in Fig. 1a,b. Using standard X-ray magnetic circular dichroism[23,24] (XMCD), we characterize the magnetic properties of doped Bi_2Se_3 films (Fig. 1c). In Mn-doped Bi_2Se_3, a hysteretic behaviour in the out-of-plane magnetic response is consistently observed, which suggests a ferromagnetically ordered groundstate. The observation

[1]Joseph Henry Laboratory, Department of Physics, Princeton University, Princeton, New Jersey 08544, USA, [2]Department of Physics, The Pennsylvania State University, University Park, Pennsylvania 16802-6300, USA, [3]Advanced Light Source, Lawrence Berkeley National Laboratory, Berkeley, California 94305, USA, [4]MAX-lab, PO Box 118, S-22100 Lund, Sweden, [5]Helmholtz-Zentrum Berlin für Materialien und Energie, Elektronenspeicherring BESSY II, Albert-Einstein-Str. 15, D-12489 Berlin, Germany, [6]Swiss Light Source, Paul Scherrer Institute, CH-5232, Villigen, Switzerland, [7]Physik-Institute, Universitat Zurich-Irchel, CH-8057 Zurich, Switzerland, [8]Department of Physics, National Tsing Hua University, Hsinchu 30013, Taiwan, [9]Institute of Physics, Academia Sinica, Taipei 11529, Taiwan, [10]Department of Physics, Northeastern University, Boston, Massachusetts 02115, USA, [11]Princeton Center for Complex Materials, Princeton Institute for Science and Technology of Materials, Princeton University, Princeton, New Jersey 08544, USA.
*e-mail: mzhasan@princeton.edu.

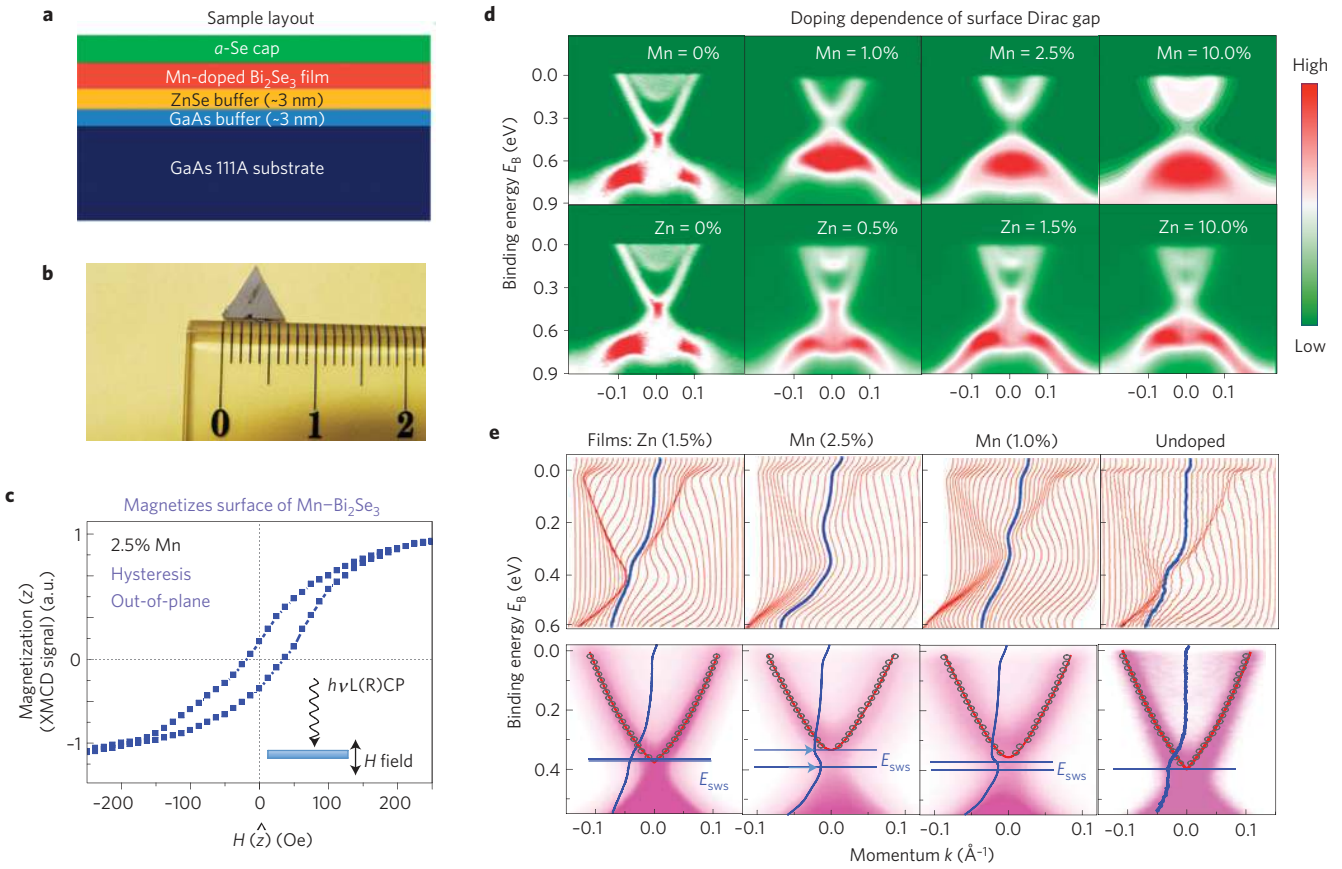

Figure 1 | Magnetic (Mn%) and non-magnetic (Zn%) doping on Bi_2Se_3 films. a,**b**, Schematic layout and photograph of MBE-grown Bi_2Se_3 films used for the experiments. **c**, Magnetization measurement at $T = 45$ K using magnetic circular dichroism shows the out-of-plane ferromagnetic character of the Mn–Bi_2Se_3 film (111) surface through the observed hysteretic response (detailed in Supplementary Section SII.5.2). Inset shows the measurement geometry. L(R)CP represents left(right)-handed circularly polarized light. **d**, Electronic band dispersion of Mn(Zn)-doped Bi_2Se_3 MBE thin films along the $\bar{M}-\bar{\Gamma}-\bar{M}$ momentum space cut. The doping level (noted in the top-right corner of each panel) reflects nominal Mn(Zn) concentration, which is defined as the ratio of Mn(Zn)/Mn(Zn) + Bi over the entire film crystal. Increasing Mn concentration leads to spectral weight suppression at the Dirac point, signalling a 'gap'. The 'gap' and the hysteresis are possibly correlated in the data. **e**, Energy-MDCs of Mn(Zn)-doped Bi_2Se_3 samples. The energy scale associated with the SWS E_{SWS} is observed as the energy spacing between the upper Dirac band minimum and the Dirac point location along the energy axis.

of ferromagnetic character and its absence in Zn–Bi_2Se_3 motivate us to systematically compare and contrast the electronic density of state behaviour in the vicinity of the surface Dirac node of these samples. Figure 1d shows the measured electronic states of Mn(Zn)-doped Bi_2Se_3 using high-resolution (spin-integrated) ARPES. In the undoped Bi_2Se_3 film (leftmost panel of Fig. 1d), a map of the spectral density of states reveals a bright and intact Dirac node (signalled by the red spot located at the Dirac crossing in the panel), which indicates that in undoped Bi_2Se_3 the Dirac node is gapless, consistent with the previous studies of pure Bi_2Se_3(ref. 25). In samples where Mn atoms are doped into the bulk (first row of Fig. 1d), we observe that the corresponding bright (red) spot at the Dirac node gradually disappears, revealing a clear systematic spectral weight suppression (SWS) with increasing Mn concentration. In contrast, the spectral intensity at the Dirac node is observed to survive on systematic Zn doping, except for the Zn = 10% sample, where some suppression of intensity is observed. This suggests that the Dirac node remains largely intact on Zn doping. The observed systematic behaviour of spectral evolution motivates us to quantitatively define an energy scale, E_{SWS}, associated with the SWS observed at the Dirac node. The value of E_{SWS} is taken as the energy spacing between the upper Dirac band minimum and the Dirac node location along the energy axis, as illustrated in Fig. 1e, which roughly corresponds to half of the surface gap magnitude. The value of the energy scale can be quantitatively determined by fitting the ARPES-measured energy-momentum distribution curves (MDCs; method described in Supplementary Section SVI). The doping dependence of E_{SWS} on samples measured at $T = 20$ K is shown in Fig. 2c. The value of E_{SWS} is observed to increase rapidly with Mn concentration, but it remains nearly zero with Zn doping. The temperature dependence of E_{SWS} is shown in Fig. 2d. The temperature induced decrease of E_{SWS} is consistent with a gradual weakening of magnetism. These observations collectively reveal a direct correlation between XMCD measured ferromagnetic character and the ARPES measured SWS (or gap) on the Mn–Bi_2Se_3 films.

Although the predominant trend in the doping evolution of surface states suggests a correlation between magnetism and SWS, we do notice a non-negligible E_{SWS} at high Zn concentration (10%). This is probably due to increasing chemical disorder on the surface of the film, because disorder degrades the surface quality. Similarly, magnetization measurements show that ferromagnetism vanishes before reaching $T = 300$ K (inset of Fig. 2b), but nonzero SWS (Fig. 2d) is still observed, perhaps, in this case, because of thermal disorder of the relaxed film surface at high temperatures. Therefore, the correlation between ferromagnetism and the ARPES gap is only clear at low temperatures in samples with reduced disorder. The momentum width (Δk) of the surface electronic states can be taken as a rough relative measure of surface disorder,

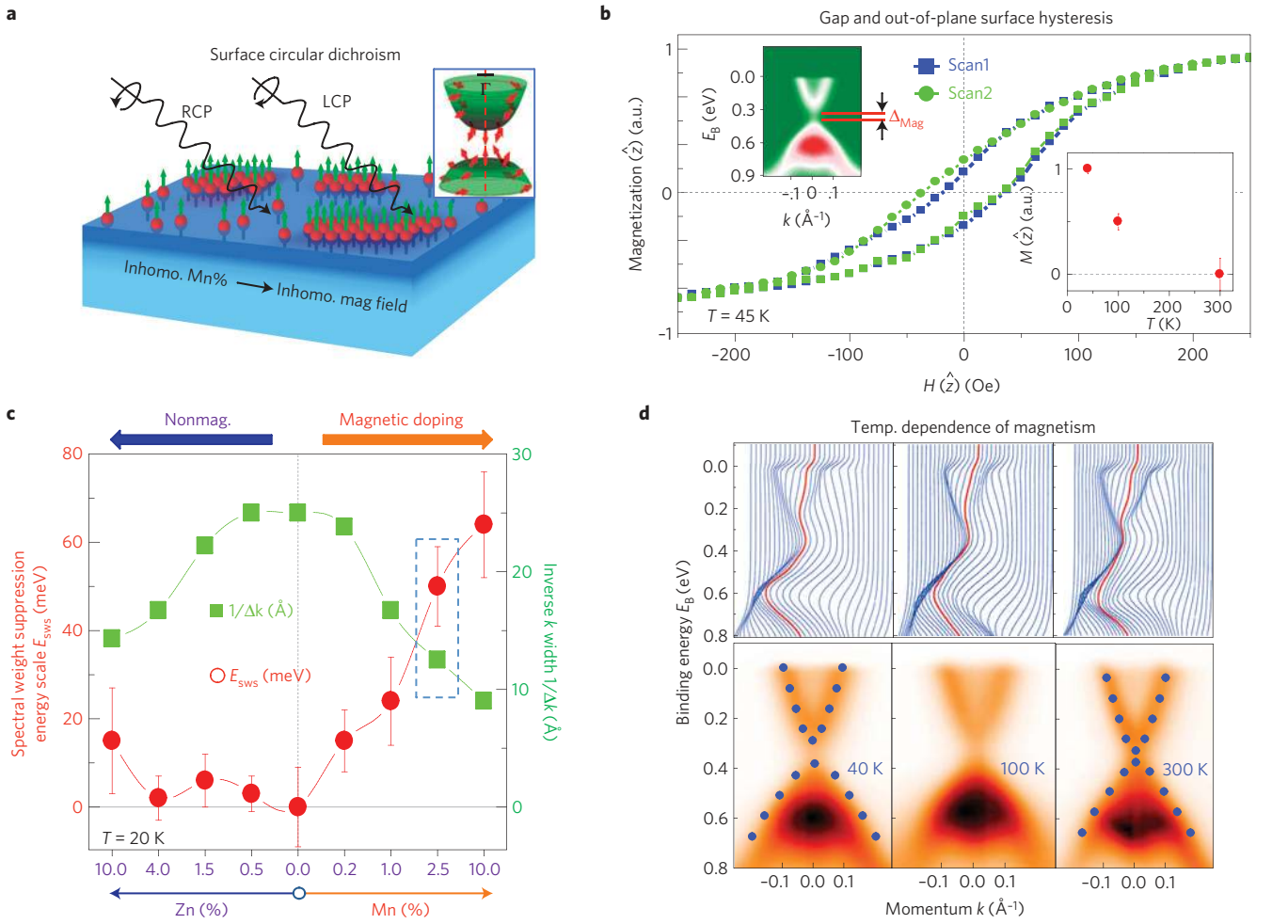

Figure 2 | Temperature and doping dependence of magnetically induced changes on Mn–Bi_2Se_3 surface. a, The Mn atoms on the surface of the film have a finite out-of-plane magnetic moment component, serving as a local magnetic field which results in the spin texture (Fig. 3) reorientation. **b**, Two independent hysteresis measurements at $T = 45$ K using XMCD reveal the ferromagnetic character of the Mn–Bi_2Se_3 film surface. The lower inset shows the remanent surface magnetization as a function of temperature. The out-of-plane magnetic hysteresis and ARPES gap were found to be correlated with each other. The upper inset shows the gap at the Dirac point in the Mn(2.5%)–Bi_2Se_3 film. **c**, The SWS energy scale E_{SWS} (defined in Fig. 1) and inverse momentum width $1/\Delta k$ of the surface states are shown as a function of Mn and Zn concentration measured at $T = 20$ K. **d**, Temperature dependence of the SWS energy scale around the Dirac point of the Mn(2.5%)–Bi_2Se_3 film (as noted in **c** by the dotted square). The value of E_{SWS} decreases as the temperature is raised, signalling a gradual weakening of the magnetism.

sample to sample, which is found to significantly increase on both magnetic and non-magnetic dopings (Fig. 2c). Strong spatial fluctuations of the surface electronic states in doped Bi_2Se_3 have been observed in recent scanning tunnelling microscope (STM) work[18], where the authors suggest the observation of gap-like feature at the Dirac point without breaking TR symmetry. These ambiguities[20] associated with the observed gap-like feature across many different experiments strongly call for critically important spin-resolved measurements which also serve as a collective method, as we show, to unambiguously identify the correct nature of the gap.

Spin configuration of the magnetic groundstate

To study the evolution of spin texture on magnetic doping, we performed spin-resolved measurements on Mn–Bi_2Se_3 topological surface states. We present two independent but representative spin-resolved ARPES measurements on Mn(2.5%)–Bi_2Se_3 film I and film II. Films I and II, both containing the same nominal Mn concentration, are measured and analysed using two different spectroscopic modes, namely, the spin-resolved MDC measurement mode and the spin-resolved energy distribution curve (spin-resolved EDC) measurement mode (see Methods), to exclude any potential systematic error in the spin measurements. Figure 3a–d shows measurements on film I. Our data shows that out-of-plane spin polarization P_z is nearly zero at large momentum $k_\parallel$ far away from the Dirac point energy ($0 < E_B < 0.1$ eV in Fig. 3c,d). On approaching the Dirac point ($0.1\text{ eV} < E_B < 0.3\text{ eV}$), an imbalance between the spin-resolved intensity in $+\hat{z}$ and $-\hat{z}$ is observed (Fig. 3c). The imbalance is found to become systematically more pronounced in the data set where scans are taken by lowering the energy toward the Dirac point. This systematic behaviour observed in the data reveals a net significant out-of-plane spin polarization in the vicinity of the 'gapped' Dirac point or near the bottom of the surface state conduction band. More importantly, the out-of-plane spin component P_z does not reverse its sign in traversing from $-k_\parallel$ to $+k_\parallel$. Such behaviour is in sharp contrast to the spin textures observed in pure Bi_2Se_3 (ref. 26), where spins point to opposite directions on opposite sides of the Fermi surface, as expected from TR symmetry. Therefore, our P_z measurements on film I near the gap edge reveal the TR breaking nature of the Mn–Bi_2Se_3 sample where magnetic hysteresis was observed using the XMCD technique. To directly measure

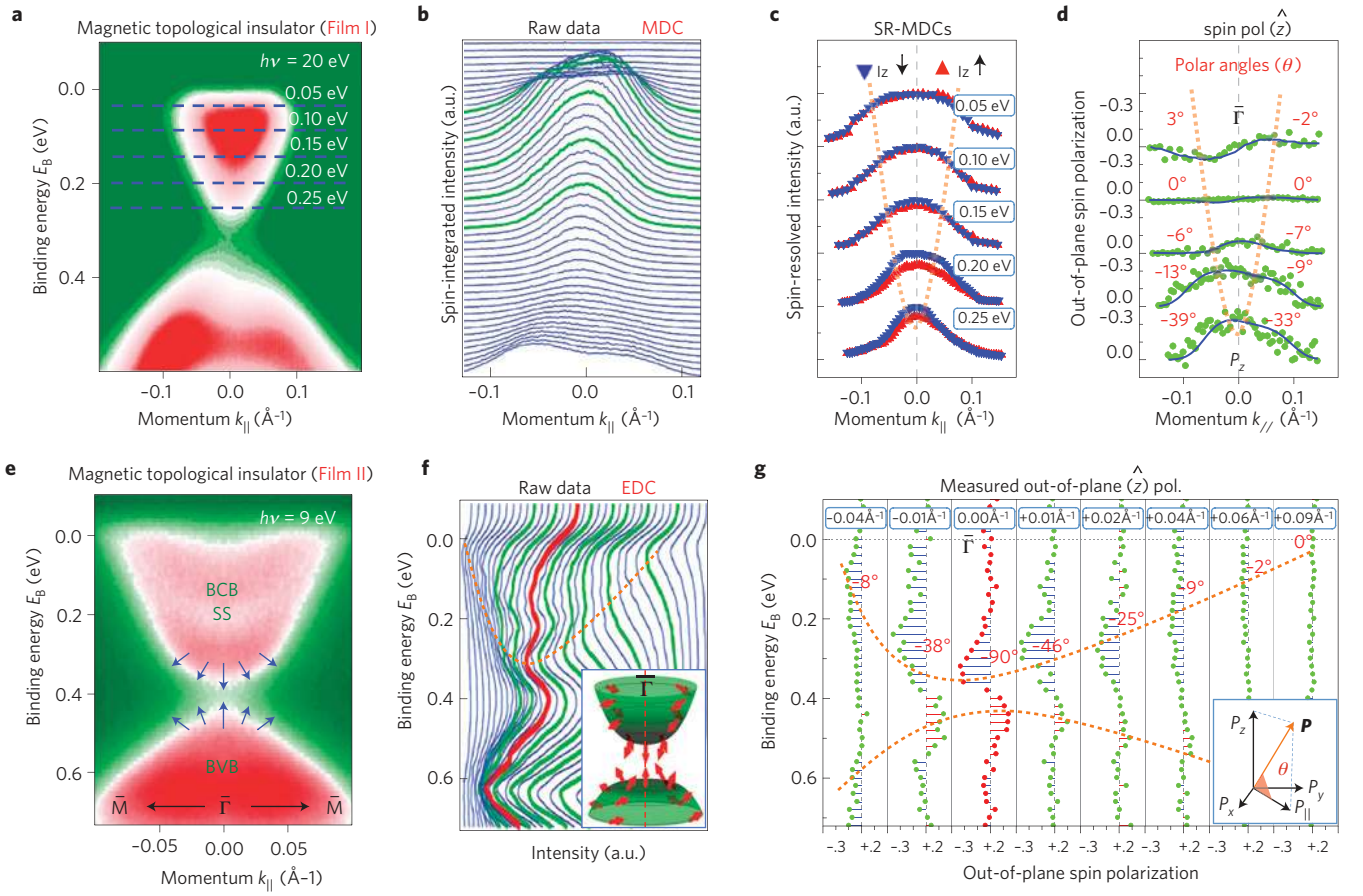

Figure 3 | Spin configuration measurements of a magnetic topological insulator. a–d Spin-resolved measurements on film I using 20 eV photons in the MDC mode. **e–g** Measurements on film II using 9 eV photons in the EDC mode. **a**,**b**, Spin-integrated data and corresponding MDCs. **c,** Spin-resolved MDC spectra for the out-of-plane direction as a function of electron binding energy. **d**, Measured out-of-plane component of the spin polarization, presented in terms of the respective out-of-plane polar angles (θ) defined in the inset of **g**. **e**,**f**, Spin-integrated dispersion and EDCs. The EDCs selected for detailed spin-resolved measurements are highlighted in green and red. **g**, Measured out-of-plane spin polarization of the EDCs corresponding to **f**. Inset defines the definition of the spin polarization vector **P** and the polar angle θ. The momentum value of each spin-resolved EDC is noted on the top. The polar angles (θ) of the spin vectors obtained from measurements are also noted. The 90° polar angle observed at $\bar{\Gamma}$ suggests that the spin vector at $\bar{\Gamma}$ momenta points in the vertical direction. The spin behaviour at $\bar{\Gamma}$ and its surrounding momentum space reveals a hedgehog-like spin configuration for each Dirac band separated by the gap, which breaks TR symmetry ($E(\mathbf{k}=0,\uparrow)\neq E(\mathbf{k}=0,\downarrow)$), as schematically shown in the inset of **f**.

the spin of the surface state at $\bar{\Gamma}$ (the Kramers' momentum, $k_{\|}=0$), we perform spin measurements on Mn–Bi_2Se_3 film II (same Mn concentration as film I) working in the spin-resolved EDC mode. The measured out-of-plane spin polarization (P_z) is shown in Fig. 3g. We focus on the P_z measurement at $\bar{\Gamma}$, the Kramers' momentum $k_{\|}=0$ (red curve): the surface electrons at TR invariant $\bar{\Gamma}$ are clearly observed to be spin polarized in the out-of-plane direction. The opposite sign of P_z for the upper and lower Dirac band (red curve in Fig. 3g) shows that the Dirac point spin degeneracy is indeed lifted up ($E(k_{\|}=0,\uparrow)\neq E(k_{\|}=0,\downarrow)$). Such an observation directly counters the Kramers' theorem and therefore manifestly breaks the TR symmetry on the surface. Next we analyse P_z measurements at finite $k_{\|}$ (green curves in Fig. 3g) to extract the detailed configuration of the spin texture. In going to larger $k_{\|}$ away from the $\bar{\Gamma}$ momenta, the measured P_z is found to gradually decrease to zero. Moreover, the constant energy momentum space plane at the Dirac point ($E_B=E_D$) is observed to serve as a mirror plane that reflects all of the out-of-plane spin components between the upper and lower Dirac bands. Thus both spin-resolved MDC (film I) and spin-resolved EDC (film II) measurement modes result in consistent conclusions regarding the spin configuration of the films. These systematic measurements, especially at the vicinity of the gap, reveal a hedgehog-like spin configuration for each upper (or lower) Dirac band separated by the magnetic gap, which breaks TR symmetry, as schematically presented in the inset of Fig. 3f (see Supplementary for further data and analysis).

Spin configurations of the non-magnetic groundstates

Spin texture measurements on non-magnetically doped films Zn(1.5%)–Bi_2Se_3 are presented in Fig. 4a–d. The out-of-plane polarization P_z measurements reveal a sharp contrast to the magnetically doped Mn–Bi_2Se_3 films, specifically, the near absence of a finite P_z component around $\bar{\Gamma}$ within our experimental resolution (Fig. 4d). A very small P_z, however, at large $k_{\|}$ is observed, which is expected because of surface state warping also observed in other TI compounds[27] (Fig. 4d). That the signal is associated with warping is further confirmed in our data because of their TR symmetric nature with P_z being observed to reverse its sign in traversing from $-k_{\|}$ to $+k_{\|}$. Moreover, our in-plane spin measurements (Fig. 4c) show that Zn–Bi_2Se_3 film retains the helical spin texture protected by the TR symmetry, as observed in pure Bi_2Se_3 and Bi_2Te_3 single crystals[26]. Therefore we conclude that non-magnetic Zn doping does not induce observable spin reorientation on the topological surface. The contrasting behaviour observed between Mn–Bi_2Se_3 and Zn–Bi_2Se_3 samples, as

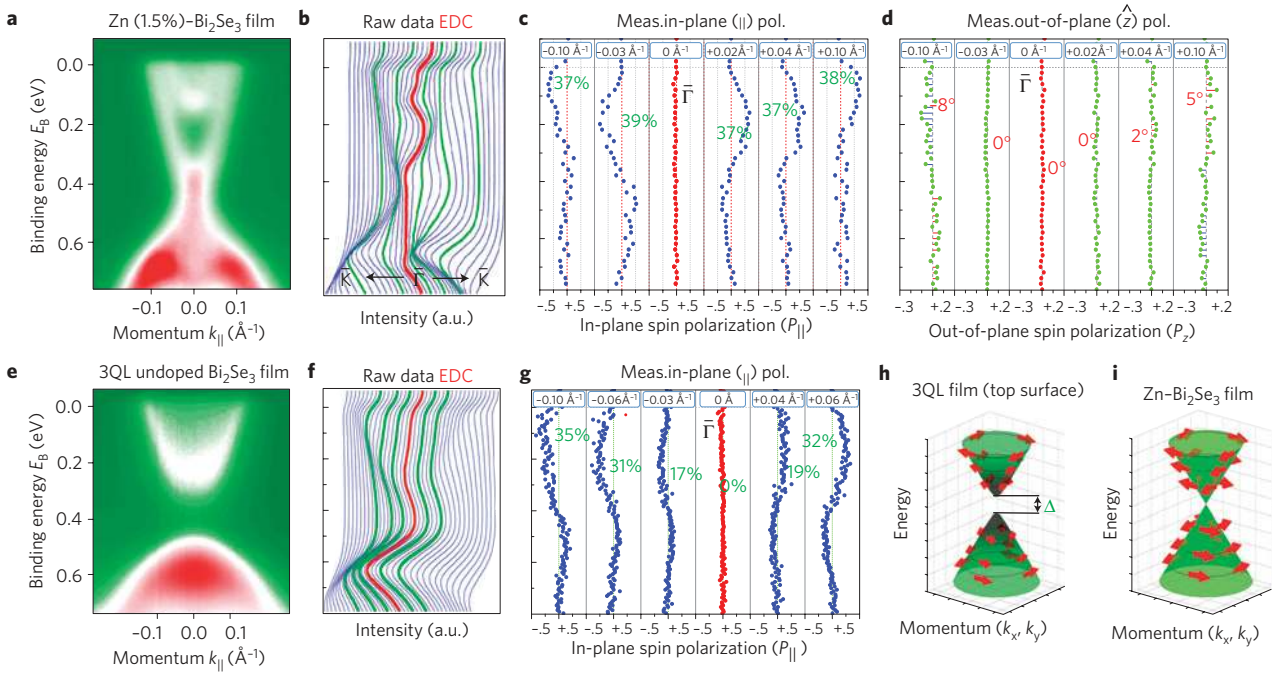

Figure 4 | Spin configurations on non-magnetic samples. a–d, Spin-resolved measurements on 1.5% non-magnetic Zn–Bi_2Se_3 film. The in-plane polarization measurements (**c**) reveal the helical spin configuration, as in pure Bi_2Se_3 TI (ref. 26, suggesting that non-magnetic impurities do not induce spin reorientation on the topological surfaces. Out-of-plane measurements (**d**) show that no significant out-of-plane spin polarization P_z is induced near the $\bar{\Gamma}$ point (the TR invariant momenta), leaving the system TR invariant overall. **e–g**, Spin-resolved ARPES measurements on ultrathin undoped Bi_2Se_3 film of three QL thickness. The net spin polarization is found to be significantly reduced near the gap edge around the $\bar{\Gamma}$ momenta. This is consistent with the fact that in ultrathin films electrons tunnel between the top and bottom surfaces. **h**,**i**, A schematic of the two types of spin texture observed in our data.

presented in Figs 3 and 4, provide clear evidence for TR symmetry breaking in Mn–Bi_2Se_3.

A surface bandgap at the Dirac point can also be generated in Bi_2Se_3 in its ultrathin film limit. In this case, the top and bottom surfaces couple together and open up a gap as electrons can tunnel from one to the other (Fig. 4e–h). Such a gap in the surfaces is not related to magnetism. It is important to know the spin configuration associated with such a gap. In Fig. 4e–h, we use spin-resolved ARPES to measure the spin configuration on the very top region (within 5 Å) of a Bi_2Se_3 film whose thickness is three quintuple layers (QL; 3 QL $\simeq$ 28.6 Å). At large parallel-momenta far away from $\bar{\Gamma}$ (for example $-0.10\,Å^{-1}$ in Fig. 4g), we observe clear spin polarization following a left-handed helical configuration with the magnitude of the polarization around 35–40%. However, in going to smaller $k_{\|}$, the magnitude of the spin polarization is observed to be reduced. At the TR invariant $\bar{\Gamma}$ momenta, spin-resolved measurements (Fig. 4g red curve) show no net spin polarization. This reduction of the spin polarization at small momenta near the gap is an intrinsic effect (Supplementary Fig. S19). These observations can be understood by considering the scenario where the surface-to-surface coupling dominates, and the two energetically degenerate surface states from top and bottom, which possess opposite helicities of the spin texture, cancel each other at $\bar{\Gamma}$ (ref. 17). This results in strong suppression of the spin polarization in the vicinity of this gap, whereas on probing momenta to large $k_{\|}$ away from $\bar{\Gamma}$, the finite kinetic energy of the surface states ($\propto vk_{\|}$) naturally leads to the spatial decoupling of two Dirac cones. These spin measurements on the ultrathin Bi_2Se_3 film reveal the interplay between quantum tunnelling (coupling) and the spin texture modification, which is of importance in spin-based device design with thin films. The observed spin texture, however, does not break TR symmetry, as the spins remain doubly degenerate at the TR invariant momenta $\bar{\Gamma}$. This is in clear contrast to the spin texture observed in Mn–Bi_2Se_3.

Magnetic contribution and geometrical phase tuning

The magnetic contribution to the gap of the Mn–Bi_2Se_3 film can be quantitatively identified using the spin texture data. The simplest **k·p** Hamiltonian that describes topological surface states under TR symmetry breaking can be written as $H = v(k_x\sigma_y - k_y\sigma_x) + b_z\sigma_z$, where σ and k are the spin and momentum operators respectively, b_z corresponds to half of the magnetic gap and v is the velocity of the surface Dirac band. We specify the out-of-plane polar angle θ of the spin polarization vector (inset of Fig. 3g) as $\theta = \arctan P_z/P_{\|}$. The magnitude of the polar angle θ reflects the competition between the out-of-plane TR breaking texture ($\propto b_z$) and the in-plane helical configuration component ($\propto vk_{\|}$). Using the measured spin-resolved data sets (θ, k), we fit the magnetic interaction strength b_z within a **k·p** scenario (see Supplementary Section SII.2). As an example, we fit b_z based on spin-resolved data sets in Fig. 3g on Mn(2.5%)–Bi_2Se_3 film II, as shown in Fig. 5c, and obtain a value of 21 meV. This is a significant fraction of the SWS energy scale observed on the same sample, $E_{SWS} > 50$ meV (see Fig. 2c for Mn = 2.5%) obtained from the spin-integrated measurements in Fig. 1c. Thus we identify the magnitude of the magnetic contribution (b_z) to the observed spectral weight suppression using spin-sensitive measurements, which suggests that the magnetic contribution is significant to E_{SWS} in Mn–Bi_2Se_3.

As demonstrated recently[28], the geometrical phase (GP) defined on the spin texture of the surface state Fermi surface[3] (also known as Berry's phase) bears a direct correspondence to the bulk topological invariant realized in the bulk electronic band structure via electronic band inversion[26,28]. We experimentally show that a GP tunability can be realized on our magnetic films, which is important to prepare the sample condition to the axion electrodynamics limit. On the Mn–Bi_2Se_3 film, the spin configuration pattern can be understood as a competition between the out-of-plane TR breaking component and the in-plane helical component of spin. The in-plane spin,

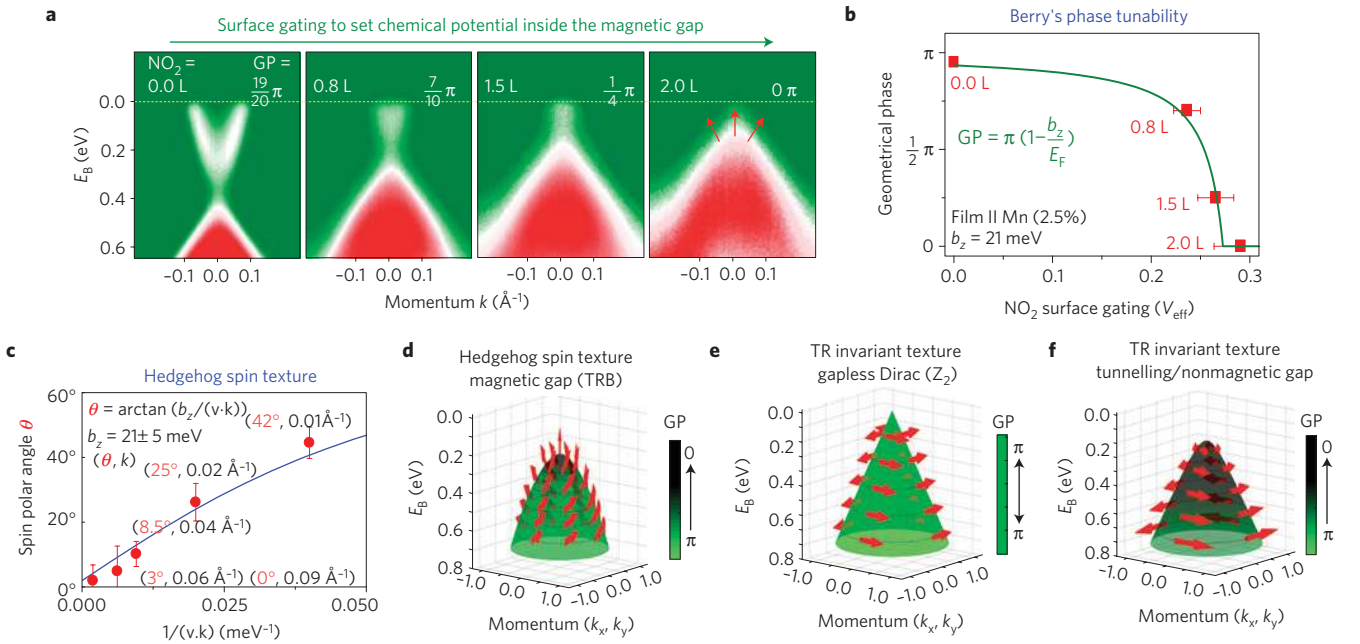

Figure 5 | Chemical potential tuned to lie inside the magnetic gap. a, Measured surface state dispersion on *in situ* NO_2 surface adsorption on the Mn–Bi_2Se_3 surface. The NO_2 dosage in Langmuir units (1.0 L = 1×10^{-6} torr s) and the tunable GP (see text) associated with the topological surface state are noted on the top-left and top-right corners of the panels, respectively. The red arrows depict the TR breaking out-of-plane spin texture at the gap edge based on the experimental data. **b**, GP or Berry's phase associated with the spin texture on the iso-energetic contours on the Mn–Bi_2Se_3 surface as a function of effective gating voltage induced by NO_2 surface adsorption. Red squares represent the GP experimentally realized by NO_2 surface adsorption, as shown in **a**. GP = 0 (NO_2 = 2.0 L) is the condition for axion dynamics. The error bars of the red squares are estimated based on the combination of the energy resolution of the ARPES experiments, the binding energy calibration with respect to the Fermi level, as well as the fitting uncertainty in fitting the ARPES measured surface states in panel **a** using the experimentally based $k\cdot p$ model. **c**, The magnetic interaction strength b_z (see text for definition), which corresponds to half of the magnetic gap magnitude, is obtained on the basis of spin-resolved data sets (polar angle θ, momentum k) for Mn(2.5%)–Bi_2Se_3 film II (Fig. 3e–g). **d**, The TR breaking spin texture features a singular hedgehog-like configuration when the chemical potential is tuned to lie within the magnetic gap, corresponding to the experimental condition presented in the last panel in **a**. **e**,**f**, Spin texture schematic based on measurements of Zn-doped Bi_2Se_3 film (60 QL), and 3 QL undoped ultrathin film with the chemical potential tuned to the Dirac point energy or within the tunnelling gap.

which can be thought of as winding round the Fermi surface in a helical pattern, contributes to a nonzero GP (ref. 26), whereas the out-of-plane TR breaking spin direction is constant as one loops around the Fermi surface and hence does not contribute to the GP. As a result, the GP remains almost π if the chemical potential lies at energies far away from the Dirac point, whereas it starts to decrease and eventually reaches zero as one approaches the TR breaking gap by lowering the chemical potential, as discussed in theory[29], at least within the magnetic energy scale b_z (Fig. 5). We show that this theoretical requirement can be experimentally achieved on the Mn–Bi_2Se_3 surface through surface NO_2 adsorption at some specific dosage level. Figure 5a shows the Mn(2.5%)–Bi_2Se_3 surface states with *in situ* NO_2 adsorption. The chemical potential is observed to be gradually shifted, and finally placed within the magnetic gap. The associated phase (GP) at each experimentally achieved sample chemical potential is found to gradually change from π to 0. The GP = 0 is the experimental condition for realizing axion electrodynamics with a TI (refs 9,11).

With the chemical potential moved into the magnetic gap, the TR breaking in-gap state features a singular hedgehog-like spin texture (Fig. 5d). Such a spin configuration, simultaneous with the chemical potential placed within the magnetic gap (Fig. 5d), is the fundamental requirement for most of the theoretical proposals relevant to the use of magnetic TIs in novel devices[5,9–12]. Furthermore, if the bulk bandgap of the Mn–Bi_2Se_3 film is tuned to zero at the critical point of the topological phase transition[28], a new topologically protected Weyl semimetal phase[30,31] with a yet more exotic but undiscovered state of matter is also predicted to take place, and is among the most exciting future frontiers to be enabled by our achievement of a sample that features a TR broken hedgehog-like spin texture with a GP = 0 state[30,31].

Methods

Sample growth. The Mn-doped Bi_2Se_3 thin films were synthesized by MBE using high-purity elemental (5N) Mn, Bi, and Se sources. A thin GaAs buffer layer was first deposited on the epi-ready GaAs 111A substrate after thermal desorption of the native oxide under As pressure. Then the substrate was transferred to another chamber, without breaking the vacuum, where a second buffer layer of ZnSe was deposited for further smoothing the surface. A Mn–Bi_2Se_3 layer (~60 nm) was then grown with a high Se/Bi beam equivalent pressure (BEP) ratio of ~15. The Mn doping concentration was controlled by adjusting the Bi/Mn BEP ratio in the range from 8 to 60. To protect the surface from oxidation, a thick Se capping layer was deposited on the Mn–Bi_2Se_3 thin film immediately after the growth. The Zn-doped Bi_2Se_3 control samples were also synthesized under the same conditions as Mn–Bi_2Se_3, with the Zn doping concentration controlled by Bi/Zn BEP. An ultrathin Bi_2Se_3 film was prepared with a thickness of 3 QL, with a typical 1 QL peak to peak variation (2–4 QL). Complete details of film growth are presented in ref. 32 and also detailed in the Supplementary Information.

Electronic structure measurements. ARPES measurements (spin-integrated) were performed with 29–64 eV photon energy on beamlines 10.0.1 and 12.0.1 of the Advanced Light Source at Lawrence Berkeley National Laboratory. Spin-resolved ARPES measurements were performed on the I3 beamline at Maxlab in Lund, Sweden, COPHEE spectrometer SIS beamline at the Swiss Light Source in Switzerland, and UE112-PGM1 beamline PHOENEXS chamber at BessyII in Berlin, Germany, using photon energies of 8–11 eV, 20–22 eV, and 55–60 eV for the three beamlines respectively. For ARPES measurements, samples were annealed *in situ* to evaporate the amorphous Se cap layer and reveal the clean surface (see Supplementary Information for further details).

Spin-resolved measurements. Spin-resolved measurements were performed using the spin-resolved ARPES beamlines mentioned above with double classical Mott detectors and linearly polarized photons. The spin-resolved measurements in Figs 3 and 4 were performed in two different modes: the spin-resolved MDC

mode and the spin-resolved EDC mode. The spin-resolved MDC mode means each single measurement measures the spin polarization at a fixed binding energy (E_B) along a certain momentum cut direction in momentum space (see Fig. 3a–d on Mn(2.5%)–Bi_2Se_3 film I). The spin-resolved EDC mode means each single measurement measures the spin polarization at a fixed momentum (k) along the binding energy axis (E_B; see Fig. 3e–g and Fig. 4 on Mn(2.5%)–Bi_2Se_3 film II, Zn(1.5%)–Bi_2Se_3 film, and 3 QL undoped Bi_2Se_3 film). Details of the spin-resolved technique and principles can be found in Supplementary Information.

Magnetic property characterizations. To cross-check the ferromagnetism implied by the spin measurements on the Mn–Bi_2Se_3 surface, XMCD was independently performed on a Mn–Bi_2Se_3 film surface at the back-endstation of the D1011 beamline at Maxlab in Lund, Sweden, with total electron yield mode at temperatures ranging from 40 K to 300 K. The XMCD measurements were performed on the L_{23} absorption edge of the Mn atom using standard methods[23] that are widely used to study the magnetic properties of transition metals and dilute magnetic semiconductor thin films or monolayers[23,24].

Detailed principles and methods of all techniques used in the experiments, including sample growth, ARPES and spin-resolved ARPES, NO_2 surface adsorption, and XMCD are further elaborated in the Supplementary Information.

Received 9 February 2012; accepted 17 May 2012; published online 24 June 2012

References

1. Hasan, M. Z. & Kane, C. L. Topological insulators. *Rev. Mod. Phys.* **82,** 3045–3067 (2010).
2. Moore, J. E. The birth of topological insulators. *Nature* **464,** 194–198 (2010).
3. Fu, L. & Kane, C. L. Topological insulators with inversion symmetry. *Phys. Rev. B* **76,** 045302 (2007).
4. Hsieh, D. *et al.* A topological Dirac insulator in a quantum spin Hall phase. *Nature* **452,** 970–974 (2008).
5. Qi, X-L., Hughes, T. L. & Zhang, S-C. Topological field theory of TR invariant insulators. *Phys. Rev. B* **78,** 195424 (2008).
6. Hor, Y. S. *et al.* Development of ferromagnetism in the doped topological insulator $Bi_{2-x}Mn_xTe_3$. *Phys. Rev. B* **81,** 195203 (2010).
7. Ji, H. W. *et al.* Bulk intergrowth of a topological insulator with a room-temperature ferromagnet $Bi_{2-x}Fe_xSe_3$. *Phys. Rev. B* **85,** 165313 (2012).
8. Salman, Z. *et al.* The nature of magnetic ordering in magnetically doped topological insulator $Bi_{2-x}Fe_xSe_3$. Preprint at http://arxiv.org/abs/1203.4850 (2012).
9. Essin, A. M., Moore, J. E. & Vanderbilt, D. Magnetoelectric polarizability and axion electrodynamics in crystalline insulators. *Phys. Rev. Lett.* **102,** 146805 (2009).
10. Garate, I. & Franz, M. Inverse spin-galvanic effect in the interface between a topological insulator and a ferromagnet. *Phys. Rev. Lett.* **104,** 146802 (2010).
11. Li, R., Wang, J., Qi, X-L. & Zhang, S-C. Dynamical axion field in topological magnetic insulators. *Nature Phys.* **6,** 284–288 (2010).
12. Yu, R. *et al.* Quantized anomalous Hall effect in magnetic topological insulators. *Science* **329,** 61–64 (2010).
13. Liu, M. *et al.* Crossover between weak localization and weak antilocalization in magnetically doped topological insulator. *Phys. Rev. Lett.* **108,** 036805 (2012).
14. Vobornik, I. *et al.* Magnetic proximity effect as a pathway to spintronic applications of topological insulators. *Nano Lett.* **11,** 4079–4082 (2011).
15. Chen, Y-L. *et al.* Massive Dirac fermion on the surface of a magnetically doped topological insulator. *Science* **329,** 659–662 (2010).
16. Wray, L. A. *et al.* A topological insulator surface under strong Coulomb, magnetic and disorder perturbations. *Nature Phys.* **7,** 32–37 (2011).
17. Zhang, Y. *et al.* Crossover of the three-dimensional topological insulator Bi_2Se_3 to the two-dimensional limit. *Nature Phys.* **6,** 584–588 (2010).
18. Beidenkopf, H. *et al.* Spatial fluctuations of helical Dirac fermions on the surface of topological insulators. *Nature Phys.* **7,** 939–943 (2011).
19. Eremeev, S. V. *et al.* The origin of 2DEG states at the surface of layered topological insulators. Preprint at http://arxiv.org/abs/1107.3208 (2011).
20. Xu, S-Y. *et al.* Dirac point spectral weight suppression, surface 'gaps', and 'twin-peak' intensity profiles in nonmagnetic and magnetic topological insulators. Preprint at http://arxiv.org/abs/1206.0278(2012).
21. Sato, T. *et al.* Unexpected mass acquisition of Dirac fermions at the quantum phase transition of a topological insulator. *Nature Phys.* **7,** 840–844 (2011).
22. King, P. D. C. *et al.* Large tunable Rashba spin splitting of a two-dimensional electron gas in Bi_2Se_3. *Phys. Rev. Lett.* **107,** 096802 (2011).
23. Nakajima, R. *et al.* Electron-yield saturation effects in L-edge x-ray magnetic circular dichroism spectra of Fe, Co, and Ni. *Phys. Rev. B* **59,** 6421–6429 (1999).
24. Edmonds, K. W. *et al.* Ferromagnetic moment and antiferromagnetic coupling in (Ga, Mn)As thin films. *Phys. Rev. B* **71,** 064418 (2005).
25. Xia, Y. *et al.* Observation of a large-gap topological-insulator class with a single Dirac cone on the surface. *Nature Phys.* **5,** 398–402 (2009).
26. Hsieh, D. *et al.* A tunable topological insulator in the spin helical Dirac transport regime. *Nature* **460,** 1101–1105 (2009).
27. Fu, L. Hexagonal warping effects in the surface states of the topological insulator Bi_2Te_3. *Phys. Rev. Lett.* **103,** 266801 (2009).
28. Xu, S-Y. *et al.* Topological phase transition and texture inversion in a tunable topological insulator. *Science* **332,** 560–564 (2011).
29. Lu, H-Z., Shi, J. R. & Shen, S-Q. Competition between weak localization and antilocalization in topological surface states. *Phys. Rev. Lett.* **107,** 076801 (2011).
30. Cho, G. Y. Possible topological phases of bulk magnetically doped Bi_2Se_3: turning a topological band insulator into the Weyl semimetal. Preprint at http://arxiv.org/abs/1110.1939(2011).
31. Halász, G. B. & Balents, L. Time reversal invariant realization of the Weyl semimetal phase. *Phys. Rev. B* **85,** 035103 (2011).
32. Zhang, D. *et al.* Interplay between bulk ferromagnetism, surface states, and quantum corrections in a magnetically doped topological insulator. Preprint at http://arxiv.org/abs/1206.2908(2012).

Acknowledgements

Work at Princeton University is supported by the US National Science Foundation Grant, NSF-DMR-1006492. M.Z.H. acknowledges visiting-scientist support from Lawrence Berkeley National Laboratory and additional partial support from the A. P. Sloan Foundation and NSF-DMR-0819860. The spin-resolved and spin-integrated photoemission measurements using synchrotron X-ray facilities are supported by the Swedish Research Council, the Knut and Alice Wallenberg Foundation, the Swiss Light Source, the Swiss National Science Foundation, the German Federal Ministry of Education and Research, and the Basic Energy Sciences of the US Department of Energy. Theoretical computations are supported by the US Department of Energy (DE-FG02-07ER46352 and AC03-76SF00098) as well as the National Science Council and Academia Sinica in Taiwan, and benefited from the allocation of supercomputer time at NERSC and Northeastern University's Advanced Scientific Computation Center. Sample growth and characterization are supported by US DARPA (N66001-11-1-4110). We gratefully acknowledge A. Preobrajenski for beamline assistance on XMCD measurements (supported by DE-FG02-05ER46200) at the D1011 beamline at Maxlab in Lund, Sweden. We acknowledge helpful discussions with S-Q. Shen and L. Balents. We also thank S-K. Mo and A. Fedorov for beamline assistance on spin-integrated photoemission measurements (supported by DE-FG02-05ER46200) at Lawrence Berkeley National Laboratory (The synchrotron facility is supported by the US DOE).

Author contributions

S-Y.X. performed the experiments with assistance from M.N., C.L., L.A.W., N.A. and M.Z.H.; D.Z., A.R. and N.S. provided samples; M.L., T.B., J.S-B., O.R., G.L., B.S., J.H.D. and J.O. provided beamline assistance; T-R.C., H-T.J., H.L. and A.B. carried out the theoretical calculations; M.Z.H. was responsible for the overall direction, planning and integration among the different research units.

Additional information

The authors declare no competing financial interests. Supplementary information accompanies this paper on www.nature.com/naturephysics. Reprints and permissions information is available online at www.nature.com/reprints. Correspondence and requests for materials should be addressed to M.Z.H.